chemosensors

MDPI

Article

Colorimetric and Fluorescence-Based Detection of Mercuric Ion Using a Benzothiazolinic Spiropyran

Ajeet Kumar, Arvind Kumar, Priya Ranjan Sahoo and Satish Kumar *

Department of Chemistry, St. Stephen's College, University Enclave, Delhi 110007, India

* Correspondence: satish@ststephens.edu

Received: 24 June 2019; Accepted: 29 July 2019; Published: 1 August 2019

Abstract: A merocyanine dye as a *p*-toluenesulfonate salt was synthesized. The structure of the dye was characterized using IR, NMR, HR-MS and single crystal X-ray crystallography. The X-ray crystallographic studies revealed the formation of a stacked aggregated structure of the merocyanine dye. The stacking interactions were investigated using the Crystal Explorer program, which estimated the strength of the interactions between different molecular pairs. The merocyanine dye was screened for affinity towards heavy metal ions, which revealed a color change from pink to colorless in the presence of mercuric ions, while other metal ions did not produce a similar change in color. In addition, the fluorescence spectroscopy indicated a change in the fluorescence intensity upon addition of mercuric ions. Both techniques displayed a good limit of detection value towards mercuric ions. In addition, the pixel intensity-based detection technique was also employed for the determination of limit of detection value with the help of a smartphone. The dynamic light scattering (DLS) studies indicated that the optical change occurred in the spectra of the receptor is due to the disaggregation of the receptor induced by mercuric ions. In addition, ^{1}H-NMR studies were also used for investigating the mechanism of interaction between the receptor and the mercuric ions. The density functional theory (DFT) studies were used to investigate the formation of the complex at the molecular level, while time dependent density functional theory (TD-DFT) studies were used to understand the observed absorption spectra through the calculation of electronic excitation parameters, which indicated an increase in the energy difference between ground and the excited state.

Keywords: colorimetric sensor; optical sensor; mercury sensor; spiropyran; merocyanine form; reversible sensors; DFT; TD-DFT

1. Introduction

Mercury pollution is known to produce devastating effects on our environment [1,2]. Although mercury is present in the earth's crust, human activities are the biggest source of mercury in our environment [3–6]. Mercury pollution originates due to the release of mercury in our environment and water bodies from a variety of sources such as coal burning, chlor-alkali, cement, plastic, medical device, electrical, paper and certain pharmaceutical industries [7–9]. In particular, polluted water bodies can seriously affect the health of a population that depends on fish consumption for their survival [10]. Mercury exists in various forms: Elemental (or metallic), inorganic (to which people may be exposed through their occupation) and organic (e.g., methylmercury, to which people may be exposed through their diet) [11,12]. Once in the environment, mercury can be transformed by bacteria into methylmercury. Methylmercury then bio-accumulates in fish and shellfish, which occurs when an organism holds higher concentrations of the element than the surroundings [13,14]. People are mainly exposed to methylmercury, an organic compound when they eat fish and shellfish that contain the compound [15,16]. These forms of mercury differ in their degree of toxicity and in

their effects on the nervous, digestive and immune systems, and on lungs, kidneys, skin, and eyes [17]. Exposure to even a small concentration of mercury can produce a number of negative health problems like minamata disease [18–20]. The world health organization considers the pollution caused by mercury among the top ten environmental problems that affect the health of humans seriously [16,21]. Owing to the hazardous effect of the presence of mercuric ions in water, it is imperative to develop sensitive and selective methods for easier detection of mercuric ions in water. Instrumental techniques such as atomic absorption spectrometry, inductively coupled plasma atomic emission spectroscopy (ICP-AES) etc. are available for the detection and determination of mercuric ions. However, instrumental techniques are expensive and non-portable and require collection and transportation of the samples for evaluation [22–24]. The monitoring of contaminated sites requires on-site evaluation of samples, which is difficult to achieve with bulky and expensive instrumentations. Therefore, there is a need to develop simple, easy and portable techniques for the detection of mercuric ions in natural water sources such as lakes and rivers. The drawback associated with instrumentation techniques may be rectified by the use of optical sensors, which are simple, portable and display optical signal in the presence of analyte [25]. In most of the analysis, the sensor molecule is the most expensive chemical species consumed during the operation, which increases the cost of the procedure. Therefore, there is a need to develop sensors, which can be reused for multiple assays. However, most of the sensors reported in the literature require harsh conditions for regeneration, which either leads to a change in the composition of the sensing material or lead to a further increase in pollution [5,26,27]. In this context, light responsive sensing materials are gaining attention as the light of a suitable wavelength can be used for their regeneration without the need for any chemical additive [28]. Among a variety of optical sensors available in the literature, the merocyanine form of spiropyran represent a family of photo-responsive molecules, which rapidly and sensitively undergoes a change in color in response to coordination with an analyte [28,29]. The spiro form, usually displays no color (non-polar form), while the merocyanine form displays an intense color (highly polar). Due to the high polarity of the merocyanine form and the presence of the phenolic oxygen atom, it usually interacts with anions or cations. In addition, the merocyanine form also displays an intense color due to the formation of H- or J- aggregates [30]. The formation or disruption of aggregation may further lead to a change in color or emission [31,32]. If this change in the aggregation properties and in turn the optical signal is induced by a metal ion, the phenomenon may be used for the detection purpose. Further, the polar nature of the merocyanine form improves the solubility of the sensor in the water. However, the merocyanine forms are usually unstable and easily transforms in the spiro form [33–35]. Therefore, the merocyanine form as a *p*-toluenesulfonate salt was synthesized and evaluated for the detection of highly toxic mercuric ions. The change in color or fluorescence signal due to the complex formation between the metal ion and the merocyanine form can be used for the determination of low concentration of analyte with the help of UV-visible or fluorescence spectroscopy. In addition, the change in color intensity can be analyzed using the digital image based colorimetric method, which is receiving increased attention owing to easy, low cost and portable analysis of a variety of samples [36–38]. The method only requires a change in color upon addition of an analyte [36]. Therefore, the use of the merocyanine form can further help in the detection of an analyte through the digital image analysis.

2. Materials and Methods

The NMR spectra were recorded using a 400 MHz *Jeol* NMR ECX 400 NMR spectrometer (Jeol USA, Inc., Peabody, MA, USA) in deuterated dimethyl sulfoxide (DMSO-d_6). The UV-Visible studies were performed on an Ocean Optics USB 4000 UV–visible spectrometer (Ocean Optics, Dunedin, FL, USA). Cary Eclipse Fluorescence spectrophotometer was used to record the fluorescence spectra keeping slit widths at 20 nm. Hydrodynamic Size (d, nm) were recorded on the Malvern ZetaSizer NanoZS DLS Instrument (Malvern Pananlytical, Malvern, UK).

2.1. Synthesis

The synthesis details of the receptor have been reported earlier [30].

2.2. UV-Visible Studies

A solution (2.2 mL) of receptor **1** (20 μM) in water buffered at pH 7.6 using 1.0 mM 4-(2-hydroxyethyl)-1-piperazineethanesulfonic acid (HEPES) was taken in a quartz cuvette to record the UV-Visible spectrum using an Ocean Optics UV-Visible spectrometer. A solution of the Hg^{2+} ions in water at pH 7.6 (1.0 mM HEPES) was gradually added to the cuvette. The UV-Visible spectra were recorded after each addition.

2.3. Procedure for Fluorescence Studies

A solution (2.2 mL) of receptor **1** (20 μM, pH 7.6, 1.0 mM HEPES in water) was taken in a quartz cuvette to record the fluorescence spectrum using the Cary Eclipse Fluorescence Spectrophotometer. A solution of the Hg^{2+} ions in water at pH 7.6 (1.0 mM HEPES) was gradually added to the cuvette. The fluorescence spectra were recorded after each addition using 365 nm excitation wavelength and 20 nm slit widths (both).

2.4. Color Intensity Measurement Studies

A solution (3.0 mL) of receptor **1** (40 μM, pH 7.6, 1.0 mM HEPES in water) was taken in vials and an increasing concentration of mercuric ion solution was added. The color photograph of the solution was taken using a smartphone device (Realme 3 pro with a 16MP camera). The photograph was analyzed for intensity using the ImageJ software [39].

Crystals: Suitable crystal was mounted at 297 K for X-ray diffraction and the data was recorded using the Xcalibur, Sapphire3 diffractometer. The details of crystal data, collection and structure refinement parameters for **1** are given in Table S1. The ShelXD/duel space program with Olex2 [40] GUI was used to solve the structure, which was further refined using the ShelXL/least square program [41]. The non-hydrogen atoms were refined anisotropically, while the hydrogen atoms like C-H (aromatic), $-CH_2$ and $-CH_3$ were placed at appropriate positions (C-H = 0.93 Å, $-CH_2$ = 0.97 Å, $-CH_3$ = 0.96 Å and treated using a riding model keeping U_{iso} (H 4C-H and $-CH_2$) = $1.2U_{eq}$(C), U_{iso} (H 4-CH_3) = $1.5U_{eq}$(C). The $-CH_3$ groups were treated as ideal rotary groups during refinement. The O-H group hydrogen atom in the structures was located at O-H = 0.82 Å and refined freely. The figures used in this paper were obtained using the Mercury software [42].

Computations: The entire computational work was performed by using the Gaussian 09 A02 software suite [43]. The initial geometries of **1** or **1**-Hg^{2+} complexes were constructed using the Gauss View 05 and optimized using the DFT/PBE1PBE/6-31+G(d) method, while the LANL2DZ basis set was used for mercury during the optimization of the complex geometries. The different stereoisomers of **1** were constructed through the rotation of three bonds that link the indole unit to the phenolic unit. The three bonds may take either a *cis* or a *trans* orientation. Based on the *cis* or *trans* orientation of the three bonds, the stereoisomers may be classified as CTC, TTC, TTT and CTT (Figure S4). The four stereoisomer CCC, CCT, TCC and TCT were not optimized due to their comparative low stability. The frequency calculations indicated the presence of a local minimum state. The most stable geometry was used to obtain the electronic excitation parameters using the DFT/PBE1PBE/6-31+G(d) method for **1** and DFT/PBE1PBE/6-31+G(d)-LANL2DZ method for the complex.

3. Results and Discussion

Synthesis: Receptor **1** was synthesized by refluxing 2,3-dimethylbenzothiazolium *p*-toluenesulfonate salt with 2-hydroxy-1-naphthaldehyde in ethanol in the presence of the catalytic amount of piperidine (Scheme 1). The product was characterized using IR, ^{1}H-, ^{13}C-NMR and HR-MS techniques as well as single crystal X-ray crystallography (Figures S1–S3).

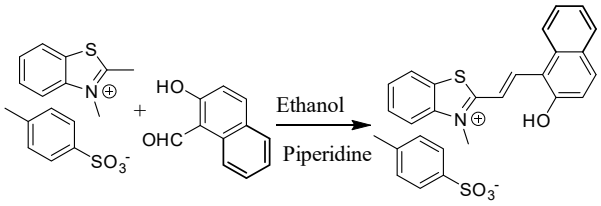

Scheme 1. The synthetic scheme for the preparation of **1**.

Crystallography: The crystals suitable for the X-ray diffraction were grown from a solution of **1** in ethanol. The crystal parameters are listed in Table S1. The asymmetric unit displayed the presence of TTC stereoisomer of the merocyanine form of **1** linked to a molecule of the *p*-toluenesulfonate group (Figures 1 and S4). The strong short contact between the oxygen atom of the *p*-toluenesulfonate group and the sulfur atom was also observed (Figure S5). In addition, the oxygen atom of the *p*-toluenesulfonate group was found to interact strongly with the aromatic C-H group (Figure S6, Table 1). The crystal packing diagram revealed the alternate arrangement of the *p*-toluenesulfonate and merocyanine unit, which leads to the formation of chains that propagate along **[**100**]** planes (Figures 2 and S7). The crystal packing revealed the presence of several short intermolecular contacts of O-H···O, O-H···S, C-H···O types (Table 1, Figures S8 and S9).

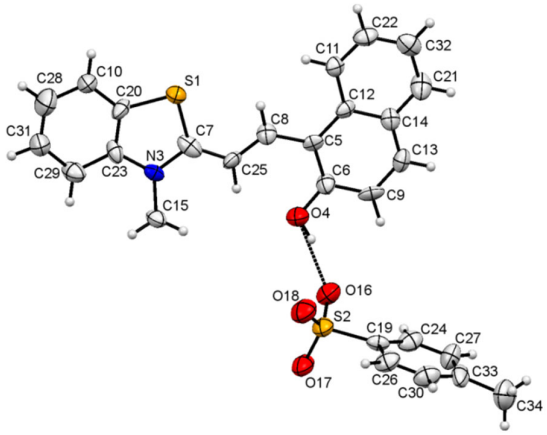

Figure 1. An ORTEP view [42] of the asymmetric unit for **1** showing the TTC unit linked to the *p*-toluenesulfonate moiety through the H-bond. Displacement ellipsoids are at 50% probability.

Table 1. Hydrogen-bond geometry (Å, °).

D—H···*A*	*D*—H	H···*A*	*D*···*A*	*D*—H···*A*
O4—H4···S2^{i}	0.92 (9)	2.66 (10)	3.520 (6)	155.0 (8)
O4—H4···O16^{i}	0.92 (9)	1.65 (9)	2.571 (7)	176.1 (9)
C15—H15B···O17^{ii}	0.96	2.54	3.433 (9)	154.4
C25—H25···O4	0.93	2.11	2.747 (9)	124.9
C29—H29···O17^{ii}	0.93	2.40	3.332 (9)	178.0

Symmetry codes: (i) $-x + 2, -y + 2, -z$; (ii) $x, -y + 3/2, z-1/2$.

The Crystal Explorer software was further used to investigate the intermolecular interactions present in **1** through the Hirshfeld surface analysis [44]. The d_{norm} function, which considers the nuclei interior (d_i), the exterior (d_e) and Van der Waal's radii (r_{vdw}) were used to map the Hirshfeld surface. The big red spots on the Hirshfeld surface indicate strong short intermolecular contacts like O···H-O and O···S-H. In addition, the π···π stacking, C-H···π, and C-H···O type interactions were also observed, which links the chains together forming aggregated chains of molecular units (Figure 3).

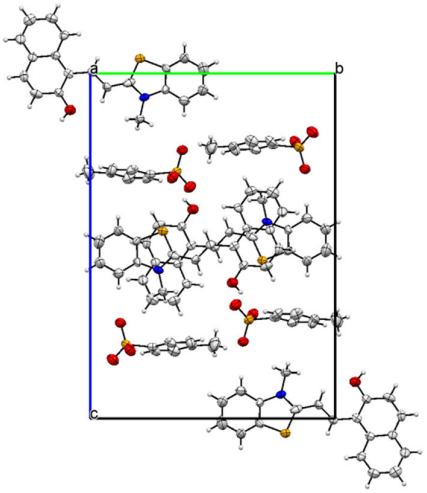

Figure 2. The crystal packing diagram of **1** viewed along axis a with displacement ellipsoid at 50% probability.

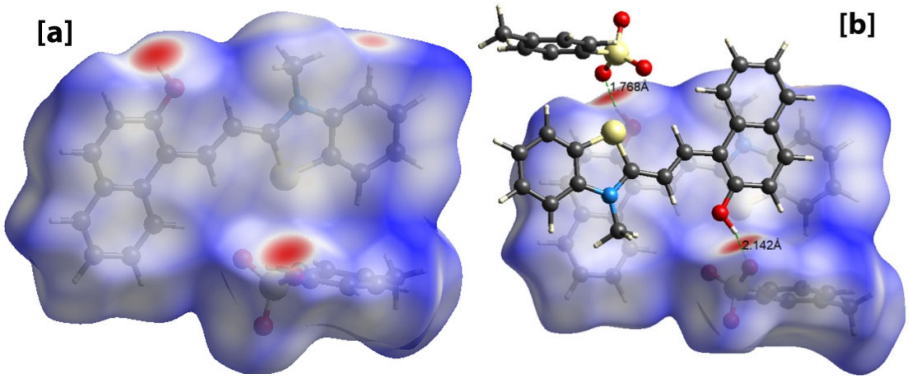

Figure 3. Hirshfeld surface analysis of **1** showing intermolecular short contacts. (a) Hirshfeld surface showing big red spots indicating strong intermolecular contacts, (b) Hirshfeld surface showing O-H···O interactions.

The 2D-Fingerprint plots obtained using the Crystal Explorer program [44,45] were used to quantitatively estimate the contribution of different type of interactions to the total Hirshfeld surface (Figures 4a and 5). The intermolecular O···H interactions, as expected, contributed significantly (21.0%) to the total Hirshfeld surface (Figure 4b). However, the major contribution to the Hirshfeld surface area emanates from π···π interactions (H···H: 44.7% and C···C 6.6%) (Figure S10). The C···H interactions also contributed significantly to the total surface area (22.0 %) (Figure S11a), while the other interactions (C···N: 1.4%, S···H: 0.9%, C···O: 0.1%, O···O: 0.3% and S···C: 3.0%) contributed to a smaller extent to the total Hirshfeld surface (Figures 5 and S11b–S13). However, the fingerprint plot indicated that the S···O interactions were insignificant to measure (less than 0.1%) (Table S2).

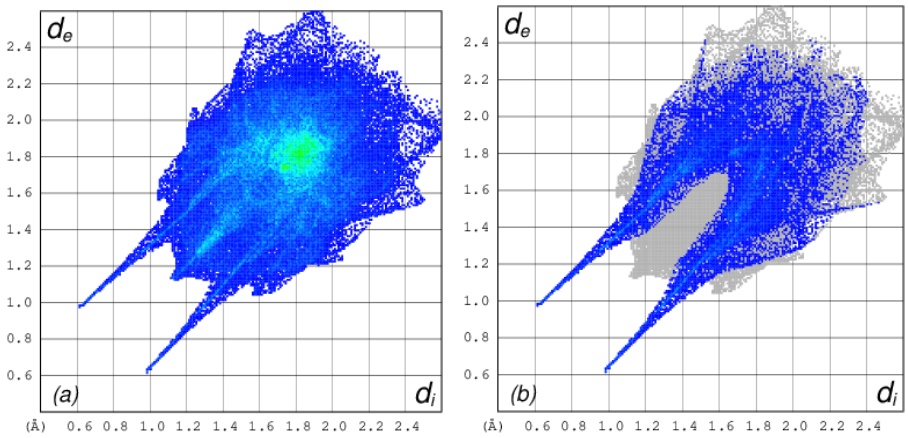

Figure 4. Two-dimensional (2D)-fingerprint plot of **1** showing (**a**) complete Hirshfeld surface; (**b**) O-H···O short contacts.

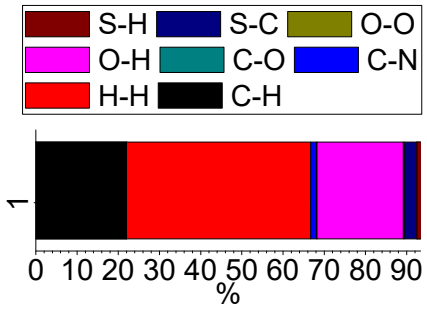

Figure 5. The percentage contribution of different intermolecular contacts to the total Hirshfeld surface.

The TONTO program in the Crystal Explorer software (B3LYP/6-31G(d,p) method was further used to estimate the energies between different molecular pairs like the central merocyanine unit and molecules surrounding it (Figures 6 and S14) [44]. The energies are listed in Table 2. The Crystal Explorer program provides the total interaction energies along with individual energy components such as electronic, dispersion, repulsion, and polarization energy. The calculations indicated −14.4 kJ/mol as total interaction energies between the *p*-toluenesulfonate moiety (*a*) and the merocyanine fragment (central unit) interacting with each other through the O···S and C-H···O type short contacts. The central merocyanine unit and the *h* moiety interacted using π···π stacking interactions to contribute −80 kJ/mol towards the stabilization of the crystal lattice. The O···H-O type H-bond between the merocyanine unit and *p*-toluenesulfonate contributed −14.8 kJ/mol towards the stabilization of the crystal lattice. The interaction energies between other molecular pairs are listed in Table 2 (Figures 6 and S14).

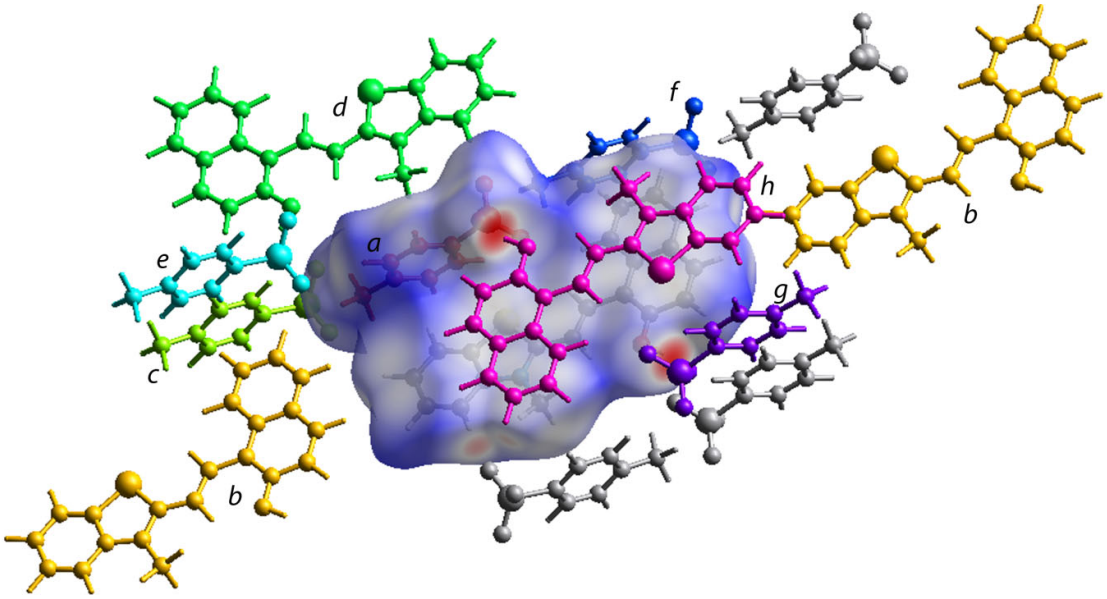

Figure 6. The Hirshfeld surface incorporating the asymmetric unit showing the interactions with the neighboring molecular units in the crystal packing. Different molecular units around the central molecule are labelled from a-h.

Table 2. The energies of interaction (kJ/mol) between the molecular pair calculated using the Crystal Explorer (TONTO) program using the B3LYP/6-31G(d,p) method.

Frag.	N	Symop	R	E_ele	E_pol	E_dis	E_rep	E_tot
a	1	-	5.42	−5.8	−4.3	−30	34	−14.4
b	1	*x*, *y*, *z*	15.3	−0.4	−0.2	−9.2	7.2	−4.1
c	1	-	13.17	0.4	−0.1	−0.3	0	0.2
d	1	*x*, −*y* + 0.5, *z* + 0.5	12.3	−0.1	−0.1	−0.9	0	−1
e	1	-	12.5	−0.1	−0.2	−0.6	0	−0.8
f	1	-	9.07	−1.3	−0.9	−13	7.8	−8.5
g	1	-	7.8	−49.8	−10.1	−13.2	92	−14.8
h	1	−*x*, −*y*, −*z*	4.07	−22.9	−9.1	−113.6	80.7	−80

3.1. Naked Eye Detection

Due to the polar nature of the merocyanine unit along with the presence of *p*-toluenesulfonate as a counter anion, **1** was screened for affinity towards toxic metal ions in water. Solutions of different metal ions and receptors were prepared in water buffered at pH 7.6 using 1.0 mM HEPES. An equivalent solution of different metal ions was mixed with a solution of **1** in water (pH 7.6, 1.0 mM HEPES). A color change to colorless was observed in a solution containing mercuric ions, while the solutions containing other metal ions displayed a faint change in color or a color change to light yellow, which indicated that **1** can be used for the visual detection of mercuric ions in water (Figure 7).

Figure 7. Color change in the solutions of receptor **1** in water (pH = 7.6, 1.0 mM HEPES) upon addition of acetate salts of various metal ions. **[1]** = 20 μM. From left to right, A = Free, B = Hg^{2+}, C = Al^{3+}, D = Cr^{3+}, E = Fe^{3+}, F = Cu^{2+}, G = Rb^{+}, H = Sm^{3+}, I = Zn^{2+}, J = K^{+}, K = Gd^{3+}, L = Pb^{2+}, M = Ca^{2+}, N = Ni^{2+}, O = Cd^{2+}, P = Fe^{2+}, Q= Mg^{2+}, R = Pd^{2+}, S = Na^{+}, T = Cs^{+}, U = Li^{+}, V = Ba^{2+}, W = Co^{2+}, X = Sr^{2+}.

3.2. UV-Visible Studies

The equimolar solutions of different metal ions and **1** in water (pH 7.6, 1.0 mM HEPES) were analyzed using the UV-Visible spectroscopy. The absorption spectra of **1** in water (pH 7.6, 1.0 mM HEPES) displayed the presence of two bands (λ_{max} = 570 nm and λ_{max} = 455 nm). The solution of mercuric ion to **1** led the disappearance of both the bands (λ_{max} = 570 nm and λ_{max} = 455 nm), with the appearance of a new absorption band with maxima at 380 nm. The addition of other metal ions (Al^{3+}, Fe^{3+}, $Cu^{2,}$ and Cr^{3+}) to the solutions of **1**, led to a decrease in the absorption band at 570 nm and a small increase in the absorption band at 455 nm (Figures 8 and S15).

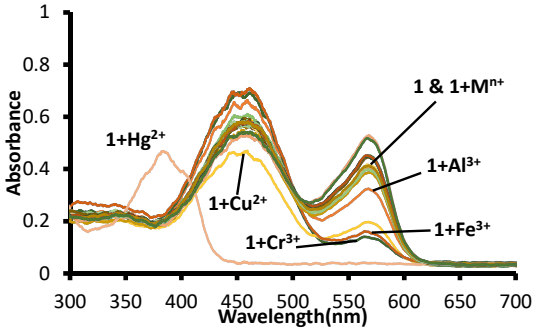

Figure 8. Change in absorption spectra of solutions of receptor **1** in water (pH = 7.6, 1.0 mM HEPES) upon addition of acetate salts of different metal ions. **[1]** 20 μM = [M^{n+}] = Hg^{2+}, Na^{+}, K^{+}, Li^{+}, Cr^{3+}, Al^{3+}, Fe^{3+}, Mn^{2+}, Ni^{2+}, Pb^{2+}, Zn^{2+}, Co^{2+}, Cu^{2+}, Cs^{+}, Ba^{2+}, Sr^{2+} ions.

A Job's plot experiment was performed to determine the stoichiometry of the complex between **1** and the mercuric ions, which displayed no clear stoichiometry. Mass spectra of a solution containing **1** and the mercuric ion was recorded in acetonitrile, it produced a strong peak at 657.1058 (Figure S16). The mass peak corresponds to $C_{24}H_{25}HgNO_6S^{+}$ (*m*/*z*: 657.1109), which correspond to a molecule of the merocyanine form linked to one mercuric ion having two acetate ions and a water molecule to complete the coordination sphere. The mass spectra indicated the formation of a 1:1 complex stoichiometry. In addition, the detection of mercuric ion by **1** was performed in the presence of one equivalent concentration of different metal ions, which indicated no significant interference (Figures S17–S19). The interference experiments indicated that mercury ions can be detected in water even in the presence of other metal ions (Figures S17–S19).

In order to further investigate the formation of a complex between **1** and metal ion, the solutions of **1** were titrated with Hg^{2+}, Fe^{3+}, $Al^{3+,}$ and Cu^{2+} ions in water at pH 7.6 (1.0 mM HEPES). The incremental addition of a solution of **1** with the Hg^{2+} ion produced a gradual decrease in the absorbance of the bands at ~450 nm and ~570 nm with simulataneous appearance of a new band at ~380 nm (Figures 9 and S20). The gradual addition of a solution of copper ions to a solution of **1** in the water at pH 7.6 (1.0 mM HEPES) produced a small decrease in the absorption band at ~455 nm and a significant decrease in the absorption band at ~570 nm (Figure S21). However, no additional peak appeared in the absorption spectra. The addition of a solution of Al^{3+}, Cr^{3+} or Fe^{3+} ions to a solution of **1** in water (pH 7.6, 1.0 mM HEPES) produced a gradual decrease in the intensity of the band ~580 nm, while no significant change in the absorption intensity at ~455 nm was observed (Figures S22–S24). The titration results were further analyzed for the calculations of the association constant between **1** and the metal ions using the HypSpec program (Figures 10 and S25–S28) [46].

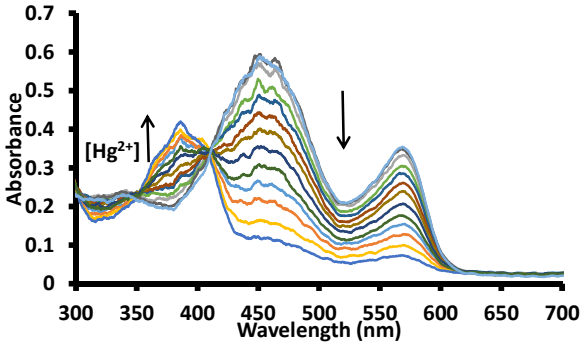

Figure 9. Change in the absorption spectra of a solution of receptor **1** in water (pH = 7.6, 1.0 mM HEPES) upon incremental addition of acetate salts of mercuric ions. The up arrow indicates an increase in absorption band intensity, while a down arrow indicates a decrease in absorption band intensity with an increase in mercuric ion concentration; **[1]** = 20 μM; [Hg^{2+}] = 0–13.63 μM.

The HypSpec program [46] utilized different binding equilibria between the host and the guest species to calculate the association constant. Therefore, different binding equilibria were used to fit the observed absorbance value with the calculated absorbance value using the HypSpec program (Figures S10 and S25–S28). The calculations that utilized 1:1 (Host:Guest) binding equilibria produced the best correlation between the observed and calculated absorbance values and yield association constant shown in Table 3.

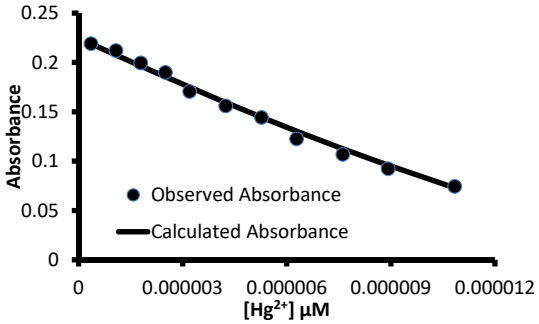

Figure 10. A correlation between the observed absorbance and absorbance value calculated using the HypSpec program for a titration between **1** and Hg^{2+} ions with 1:1 (H:G) binding stoichiometry.

Table 3. The binding constant value obtained for a 1:1 (H:G) binding stoichiometry and changes observed at a different wavelength for **1** with different metal ions.

Metal	Logβ11	Change in λ_{max} (nm) at
Hg^{2+}	5.2480 ± 0.0229	380, 450, 570
Cu^{2+}	5.0172 ± 0.0193	455, 564
Al^{3+}	4.8992 ± 0.0504	563
Cr^{3+}	4.8949 ± 0.0075	564
Fe^{3+}	4.59582 ± 0.0307	563

3.3. Fluorescence Studies

The aggregated solution of the merocyanine form is known to display a change in fluorescence intensity upon addition of an analyte. Therefore, equimolar solutions of **1** and metal ions were investigated for change in emission spectra using 570 nm, 450 nm, and 365 nm excitation wavelengths in the water at pH 7.6 (1.0 mM HEPES). A very faint fluorescence signal was observed using 450 nm and 570 nm excitation wavelengths in a solution of **1** and **1** with metal ions. However, an equimolar solution of **1** and mercuric ion displayed a strong emission band at 425 nm with a

45 nm Stokes shift using a 365 nm excitation wavelength (Figures 11 and S29). The equimolar solution of **1** and mercuric ion displayed a 27 fold enhancement in the fluorescence intensity in comparison to the fluorescence intensity displayed by a solution of **1** in water (Figure 11). However, no change in the fluorescence intensity was observed for solutions containing **1** and other metal ions.

Further, a titration experiment was conducted between a solution of **1** and mercuric ions in water at pH 7.6 (1.0 mM HEPES) using a 365 nm excitation wavelength at 20 nm slit width. The gradual addition of a solution of mercuric ions produced a gradual increase in the fluorescence intensity at 425 nm (Figure 12).

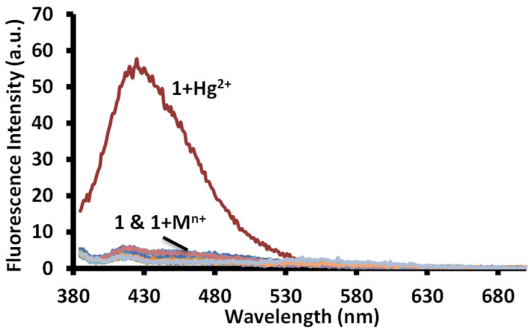

Figure 11. Change in fluorescence spectra of solutions of receptor **1** in water (pH = 7.6, 1.0 mM HEPES) upon addition of acetate salts of different metal ions. **[1]** = 20 μM = $[M^{n+}]$ = Hg^{2+}, Na^{+}, K^{+}, Li^{+}, Cr^{3+}, Al^{3+}, Fe^{3+}, Mn^{2+}, Ni^{2+}, Pb^{2+}, Zn^{2+}, Co^{2+}, Cu^{2+}, Cs^{+}, Ba^{2+}, Sr^{2+} ions.

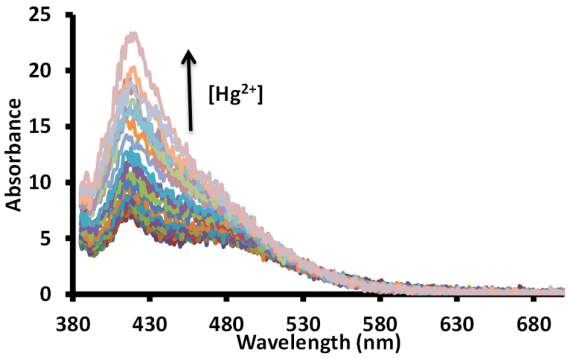

Figure 12. Change in fluorescence spectra of a solution of receptor **1** in water (pH=7.6, 1.0 mM HEPES) upon incremental addition of acetate salts of mercuric ions. The up arrow indicate an increase in intensity with an increase in mercuric ion concentration; **[1]** = 20 μM; $[Hg^{2+}]$ = 0–0.67 μM.

3.4. DLS Studies

The solid-state solution of **1** displayed the presence of networks of molecular chains linked through H-bonds. In addition, the solution of **1** displayed an absorption band near 570 nm, which indicated that it may be present in the aggregated form (J-aggregation) [32]. Therefore, dynamic light scattering experiments were performed for solutions of free **1** and **1** containing different metal ions, which produced a change in absorption spectra. A solution of **1** displayed a mean particle size of 535 nm. The addition of one equivalent mercuric ion to a solution of **1** produced a decrease in the mean particle size of 168 nm. A similar decrease in the particle size was also observed in an equimolar solution of copper ions and **1**. However, a solution of aluminum (~1594 nm) and chromium (851 nm) displayed an increase in the mean particle size, which indicated that the decrease in the absorbance at 455 nm and 470 nm is due to dis-aggregation, while a decrease in the absorbance at 470 nm only, indicate stronger aggregation. The experiment further indicates that mercury and copper ions cause dis-aggregation of **1**, while ferric, aluminum and chromium ions induce aggregation in **1** (Figure 13).

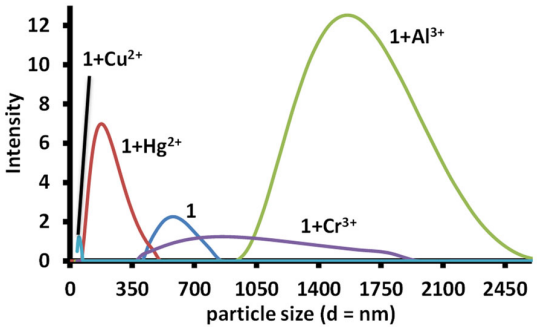

Figure 13. The particle size observed in a solution of **1**, **1**-Hg^{2+} (1:1), **1**-Cr^{3+} (1:1), **1**-Al^{3+} (1:1) and **1**-Cu^{2+} (1:1) in water; **[1]** = $[Hg^{2+}]$ = $[Cr^{3+}]$ = $[Al^{3+}]$ = $[Cu^{2+}]$ = 1.02 mM.

3.5. NMR Studies

In order to investigate the formation of a complex between the mercuric ions and **1**, the ^{1}H-NMR spectra of **1**, **1**-Hg^{2+} and **1**-Al^{3+} were recorded in DMSO-d_6 (Figures 14 and S30). Due to the paramagnetic effect associated with the copper, ferric and chromium ion solutions, the ^{1}H-NMR of their complex was not recorded. The ^{1}H-NMR of **1** indicated the alkene proton (H7 and H8) at δ8.59 and δ8.18 ppm (Figure 14). The OH group signal was observed at δ11.79 ppm. The NCH_3 group signal was observed at δ4.24 ppm, which indicated the presence of the merocyanine form of **1** in the solution. The addition of mercuric ion to a solution of **1** produced an upfield shift in the signal due to aromatic and aliphatic protons. The signal due to proton H1 shifted from δ7.35 ppm to δ6.57 ppm, which indicated the absence of hydrogen atom attached to the phenolic oxygen atom. The signal due to proton H9 shifted from δ8.39 to δ6.97 ppm, which indicated a reduction in the positive charge on the nitrogen atom. Similarly, signals due to other protons in the indole ring also shielded owing to a reduction in the positive charge on the nitrogen atom. The N-CH_3 signal also shielded and shifted from δ4.24 ppm to δ2.86 ppm upon addition of the mercuric ion (Figure S30). The mass spectra produced no peak due to a dimerized form of **1**. The ^{1}H-NMR also indicated the absence of the closed form of **1**. Therefore, the analysis of ^{1}HNMR indicated the formation of a complex, where the mercuric ion is linked to the quinoidal form of **1** through the phenolic oxygen atom [47]. The ^{1}H-NMR of **1**-Al^{3+} complex indicated the absence of a significant shift in the signal due to aromatic or aliphatic protons (Figures S31 and S32). A small and insignificant shift in the signals due to different protons indicated that the complex formation between the aluminum ion and **1** may lead to a change in the aggregation state only.

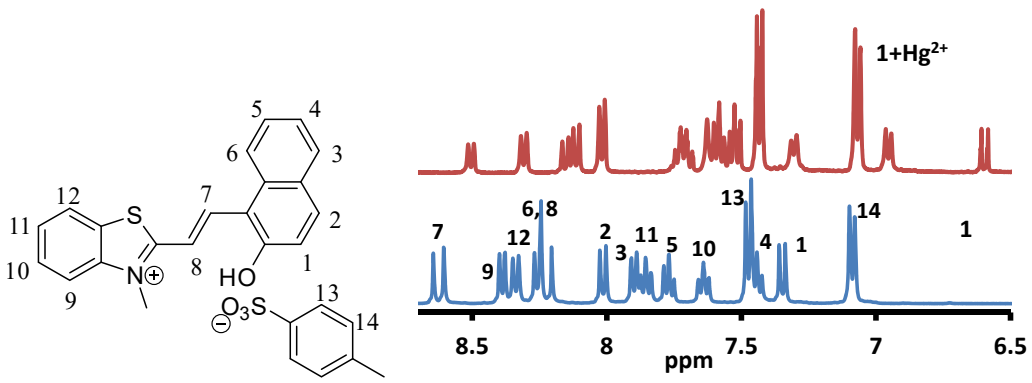

Figure 14. Partial ^{1}H-NMR spectra of **1** and **1**-Hg^{2+} in DMSO-d_6 recorded on a 400 MHz instrument showing a comparison in the aromatic region.

3.6. Practical Utility

For any practical utility of **1** for the detection of mercuric ions, it is imperative to determine the limit of detection value. Therefore, the limit of the detection value of **1** towards mercuric ions was determined using UV-Visible and fluorescence spectroscopies with the help of the $3\sigma/m$ equation. A straight line curve was observed between the absorbance (570 nm) and the concentration of mercuric ions. Similarly, a straight line curve was observed between the fluorescence intensity at 424 nm and the mercuric ion concentration (Figures 15 and S33). The UV-Visible data yielded 0.32 μM as the limit of detection value for **1** towards mercuric ions, while 67.8 nM limit of detection values for **1** towards mercuric ion was observed using fluorescence data.

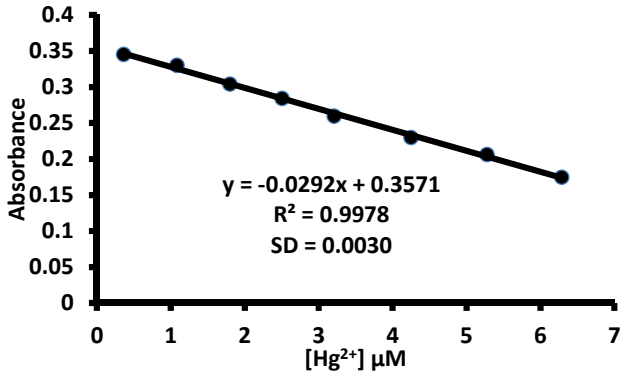

Figure 15. The determination of limit of the detection value of 1 towards mercuric ions using ultra violet (UV)-Visible spectroscopy.

The detection limit was further established using the color intensity measurement method. For on-field utilization of any sensor for the detection of toxic metal ion, it is essential to carry out the analysis using simple devices. Therefore, color photographs of solutions taken using a smartphone followed by their color intensity analysis with the software can be useful for on field measurement of toxic metal ion concentration in water samples (Figure 16). The solutions of **1** containing a different concentration of mercuric ions were prepared. The digital images of the solutions were analyzed using the ImageJ software (Figure 16). The pixel intensity of the solution versus the concentration of mercuric ion was plotted, which yielded a straight line. The straight line plot yielded 89.4 nM as the limit of the detection value of **1** towards mercuric ions. The limit of detection value observed through the color intensity measurement was found to be better than obtained using the UV-visible spectroscopy.

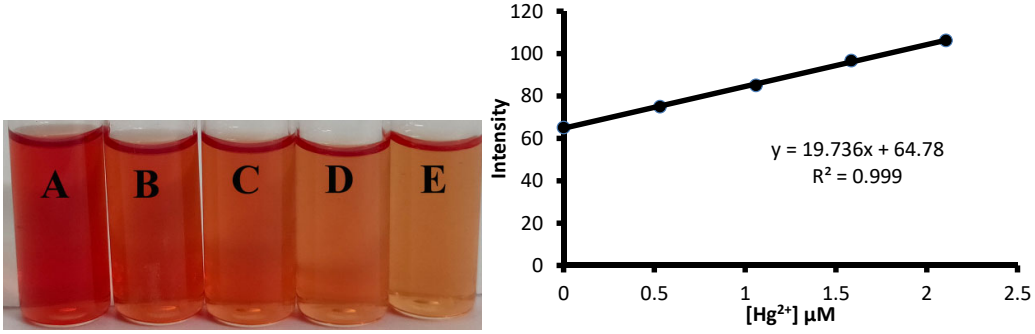

Figure 16. The determination of limit of detection value of **1** towards mercuric ions using the solution intensity method. (**Left**) Concentration of Hg^{2+} ion in: A = 0.0 μM; B = 0.53 μM; C = 1.06 μM; D = 1.58 μM; E = 2.10 μM. (**Right**) A graph showing the change in pixel intensity of the solution with an increase in the mercury ion concentration.

Further, filter paper test strips were prepared from the Whatman filter paper and dipped into a solution of **1** in acetonitrile. The filter paper strips after drying in the air were dipped in the solutions of different metal ions. A filter paper strip dipped in a solution of mercuric ion decolorized, while filter paper strips dipped in the solutions of ferric and chromium ions displayed a yellow color. A small, insignificant change in the color was observed on filter paper strips dipped in solutions containing other metal ions (Figure 17). The experiment indicated that **1** can be used for the detection of mercuric ions in water.

Figure 17. Color change on paper strips coated with the receptor **1,** dipped in the solutions of acetate salts of various metal ions. [**1**] = 20 μM. From left to right, A = Free, B = Hg^{2+}, C = Al^{3+}, D = Cr^{3+}, E = Fe^{3+}, F = Cu^{2+}, G = Rb^{+}, H = Sm^{3+}, I = Zn^{2+}, J = K^{+}, K = Gd^{3+}, L = Pb^{2+}, M = Ca^{2+}, N = Ni^{2+}, O = Cd^{2+}, P = Fe^{2+}, Q = Mg^{2+}, R = Pd^{2+}, S = Na^{+}, T = Cs^{+}, U = Li^{+}, V= Ba^{2+}, W = Co^{2+}, X = Sr^{2+}.

3.7. Computational Studies

In order to understand the complex formation between **1** and mercuric ions, the PBE1PBE(PBE0)/6-31+G(d) method was used with the Gaussian program suite [43]. Due to the presence of a number of short contacts in **1**, the PBE0 method was chosen as it yields good results with noncovalent interactions during the calculations [48]. The geometries of **1** in the TTT, TTC, CTC and CTT stereo-isomeric forms were optimized. The calculations indicated that the TTC form is the most stable stereo-isomeric of **1** (Table 4, Figures 18 and S34).

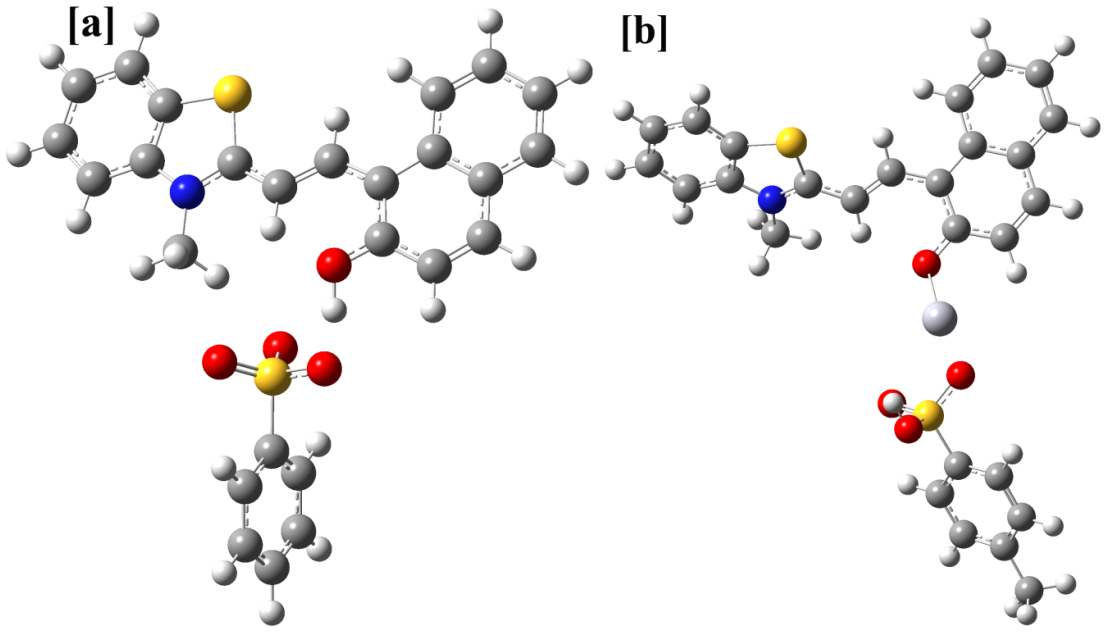

Figure 18. The DFT/PBE1PBE/6-31G(d)/LANL2DZ optimized geometries of the most stable form of **1** and its complex with mercuric ion. (a) the geometry of the TTC form linked to a *p*-toluenesulfonate group, (b) the geometry of the TTC-Hg^{2+} complex.

Table 4. The calculated total and relative energies (kcal/mol) calculated using the PBE1PBE/631+G(d) method.

Stereo-Isomer	E_1 [a]	E_2 [b]	E_3 [c]	$E_{rel} = E_{TTC} - E_{SI}$ [d]	E_{1+Hg}	E_{rc} [f]	$\Delta E = E_{1\text{-}Hg^{2+}} - (E_3 + E_{Hg^{2+}})$
TTC	−814,597.26	−814,854.47	−1,376,038.65	0	−1,402,460.35	0	−195.90
CTT	−814,599.01	−814,849.28	−1,376,032.66	5.98	−1,402,457.10	3.24	−198.64
CTC	−814,602.62	−814,851.30	−1,376,032.18	6.47	−1,402,457.77	2.57	−199.79
TTT	−814,595.80	−814,852.95	−1,376,031.82	6.82	−1,402,460.04	0.31	−202.41

[a] isomers shown in Figure S35; [b] isomer shown in Figure S36; [c] isomers shown in Figures 18 and S34 [d] ESI is the energy of different stereoisomers of **1**. [f] E_{rc} is the relative energy with respect to the energy of the TTC-Hg complex.

The DFT/PBE1PBE/6-31+G(d)/LANL2DZ method was further used to optimize the geometry of the complex between different stereoisomers of **1** and mercuric ion. The different geometries of the complex with and without *p*-toluenesulfonate were optimized. The geometries having the *p*-toluenesulfonate group as the coordinating group were observed to be more stable than the geometries, which were optimized without this moiety. However, it may be interacting weakly with the mercuric ion. Further, the position of the hydrogen atom that links the *p*-toluenesulfonate group and the merocyanine form was also established using DFT calculations. For, the TTC isomer, the combined energy of the *p*-toluenesulfonic acid and the unprotonated form of merocyanine (TTC) was compared with the combined energy of the *p*-toluene sulfonate and protonated form of the merocyanine (TTC+H), which indicated that the former is more stable than the latter by −63.84 kcal/mol. Further, a comparison of the energy of the different complex geometry indicated that the TTC isomer forms the most stable complex with the mercuric ion (Table 4, Figures S35–S37). In addition, the combined energy of the different stereoisomer of **1** and Hg^{2+} ion was compared with the energy of the stereoisomer-Hg^{2+} complex, which indicated higher stability of the complex in comparison to the reactants (Table 4). Further, calculations indicated that the TTT isomer should form the complex much more readily than the other stereoisomers of **1** (Table 4, Figures S35–S37). The PBE1PBE/6-31+G(d) optimized the geometry of the most stable stereoisomer of **1** (TTC) was further used for the calculation of excitation parameters using the TD-DFT/PBE1PBE/6-31+G(d) method. The calculation indicated that the transition between HOMO to LUMO orbitals (So to S1) is responsible for the observed absorption band in **1** (Figure 19, Table S3). The most stable geometry of the **1**-Hg complex was used to calculate the excitation parameters using the TD-DFT/PBE1PBE/6-31+G(d) method, which suggested that HOMO to LUMO+1 and HOMO-1 to LUMO+1 orbitals are responsible for the observed singlet electronic observed in **1** (Figure 19). The electronic excitation parameters are given in Table S3. The TD-DFT calculations indicated that there is an increase in the ground state to the excited state gap, which causes a hypsochromic shift.

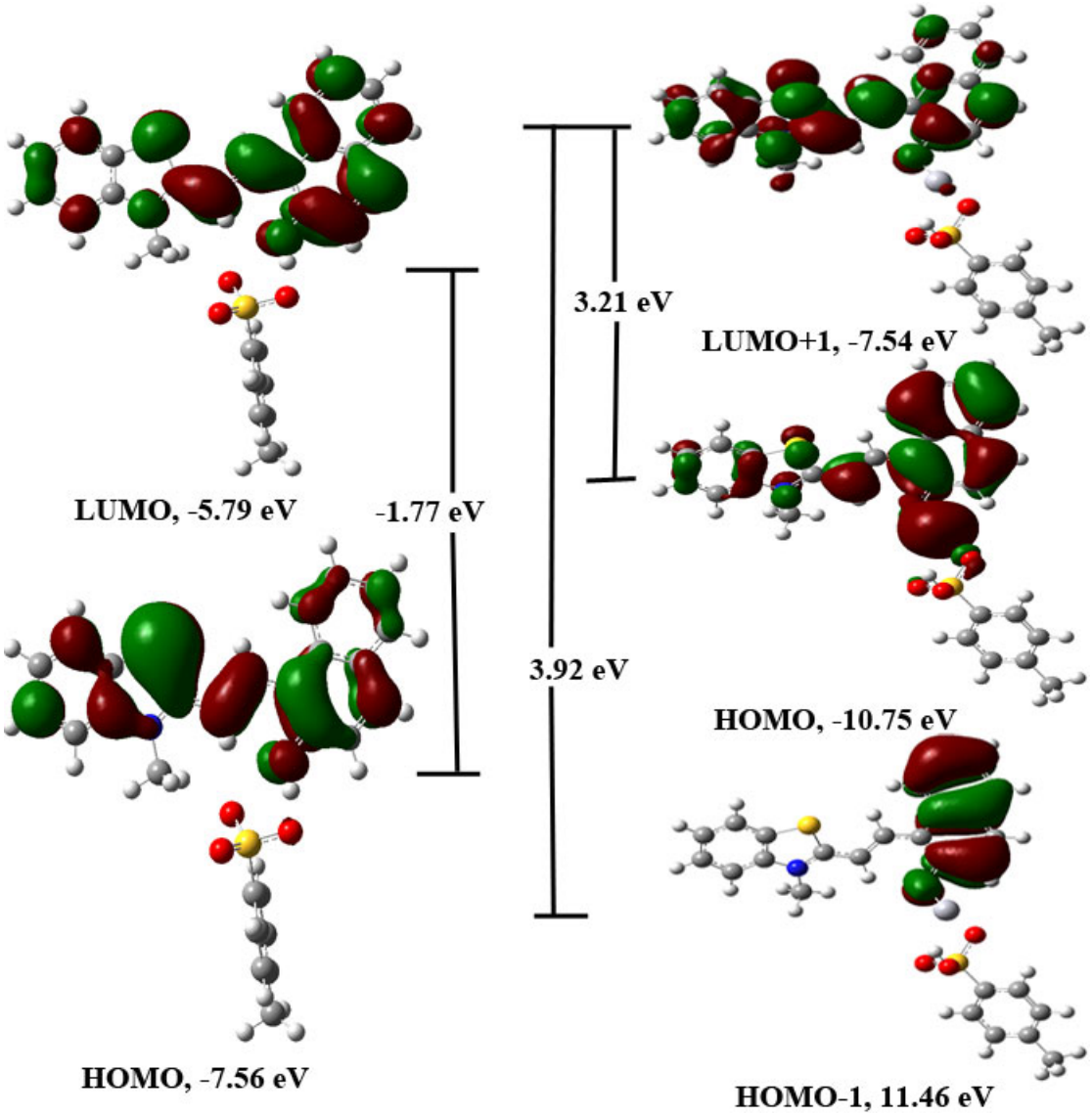

Figure 19. The TD-DFT/PBE1PBE/6-31+G(d)/LANL2DZ calculated energy diagram of **1** and **1**-Hg^{2+} complex showing main orbitals involved in the transition.

4. Conclusions

In summary, the structure of the merocyanine form was established using the single crystal X-ray crystallography to reveal extensive H-bonding that led to the formation of aggregates. The energy of the interactions was determined. The merocyanine form detected the presence of mercuric ions in water through the disaggregation mechanism and displayed a change in color visible to the naked eye (pink to colorless). The trivalent metal ions like chromium, aluminum, and ferric ions caused further aggregation of the merocyanine form. The association constant values were calculated, which indicated the formation of a complex between the mercuric ion and the merocyanine form. The lower value of the association constant was observed with trivalent metal and copper ions. The complex between the receptor and mercuric ion displayed a fluorescence response. Both UV-visible and fluorescence studies provided a good limit of the detection value of the receptor towards mercuric ions. Further, the limit of the detection value was obtained from a solution of the receptor and mercuric ion using the pixel intensity analysis, which provided a better limit of detection value in comparison to the UV-Visible spectroscopic analysis. It was demonstrated that the image pixel analysis can provide a better limit of the detection value of **1** for mercuric ions. DLS studies

demonstrated the disaggregation of the merocyanine form in the presence of the mercuric ion. The ^{1}H-NMR further indicated the formation of a complex between the merocyanine form and the mercuric ion. The DFT studies indicated that the TTC form is the most stable stereoisomeric form of the receptor. The TD-DFT studies indicated that the addition of the mercuric ion increases HOMO and LUMO gap in the receptor, which support the experimental results.

Supplementary Materials: The following are available online at www.mdpi.com/xxx/s1, Figure S1: The ^{1}H-NMR of **1** recorded in DMSO-d_6 on a 400 MHz instrument, Figure S2: The ^{13}C-NMR of **1** recorded in DMSO-d_6 on a 400 MHz instrument, Figure S3: HR-MS of **1**, Figure S4: The structure of different stereoisomers of **1**, Figure S5: The crystal structure of **1** showing O···S and C-H···O interactions, Figure S6: The crystal structure of **1** showing O···S interaction, Figure S7: The crystal packing diagram of **1** viewed along b-axis showing the packing of receptor units in the lattice with the help of H-bonds, Figure S8: The crystal packing diagram of **1** viewed along a-axis showing short intermolecular contacts, Figure S9: The crystal packing diagram of **1** viewed along b-axis showing short intermolecular contacts, Figure S10: 2D Fingerprint plots of **1** showing (a) C···C (b) H···H contacts, Figure S11: 2D Fingerprint plots of **1** showing (a) C···H (b) C···O contacts, Figure S12: 2D Fingerprint plots of **1** showing (a) S···H and (b) S···C contacts, Figure S13: 2D Fingerprint plots of **1** showing (a) C···N (b) O···O contacts, Figure S14: The interaction of central merocyanine unit with other molecular units obtained using Crystal Explorer program, Figure S15: An expanded view of the change in absorption spectra of solutions of receptor **1** in water (pH=7.6, 1.0 mM HEPES) upon addition of acetate salts of different metal ions. [**1**] = 20 μM = [M^{n+}] = Hg^{2+}, Na^{+}, K^{+}, Li^{+}, Cr^{3+}, Al^{3+}, Fe^{3+}, Mn^{2+}, Ni^{2+}, Pb^{2+}, Zn^{2+}, Co^{2+}, Cu^{2+}, Cs^{+}, Ba^{2+}, Sr^{2+} ions, Figure S16: The HR-MS of a solution of **1**-Hg^{2+} prepared in acetonitrile, Figure S17: The bar chart drawn at 375 nm for **1** (20 μM) upon addition of one equivalent mercuric ion and one equivalent different metal ions to a solution of **1** in water (1.0 mM HEPES, pH 7.6), Figure S18: Color change in the solutions of receptor **1** (20 μM) in water (pH = 7.6, 1.0 mM HEPES) upon addition of acetate salts of various metal ions in the presence of same concentration of other metal ion. [**1**] = 20 μM. From left to right, A = Free, B= Hg^{2+}, C = Hg^{2+} + Al^{3+}, D = Hg^{2+} + Cr^{3+}, E = Hg^{2+} + Fe^{3+}, F = Hg^{2+} + Cu^{2+}, G = Hg^{2+} + Rb^{+}, H = Hg^{2+} + Sm^{3+}, I = Hg^{2+} + Zn^{2+}, J = Hg^{2+} + K^{+}, K = Hg^{2+} + Gd^{3+}, L = Hg^{2+} + Pb^{2+}, M = Hg^{2+} + Ca^{2+}, N = Hg^{2+} + Ni^{2+}, O = Hg^{2+} + Cd^{2+}, P = Hg^{2+} + Fe^{2+}, Q = Hg^{2+} + Mg^{2+}, R = Hg^{2+} + Pd^{2+}, S = Hg^{2+} + Na^{+}, T = Hg^{2+} + Cs^{+}, U = Hg^{2+} + Li^{+}, V = Hg^{2+} + Ba^{2+}, W = Hg^{2+} + Co^{2+}, X = Hg^{2+} + Sr^{2+}, Figure S19: Color change on paper strips coated with the receptor **1,** dipped in the solutions of acetate salts of various metal ions in the presence of same concentration of other metal ion. [**1**] = 20 μM. From left to right, A = Free, B= Hg^{2+}, C=Hg^{2+} + Al^{3+}, D = Hg^{2+} + Cr^{3+}, E = Hg^{2+} + Fe^{3+}, F = Hg^{2+} + Cu^{2+}, G = Hg^{2+} + Rb^{+}, H = Hg^{2+} + Sm^{3+}, I = Hg^{2+} + Zn^{2+}, J = Hg^{2+} + K^{+}, K = Hg^{2+} + Gd^{3+}, L = Hg^{2+} + Pb^{2+}, M = Hg^{2+} + Ca^{2+}, N = Hg^{2+} + Ni^{2+}, O = Hg^{2+} + Cd^{2+}, P = Hg^{2+} + Fe^{2+}, Q = Hg^{2+} + Mg^{2+}, R = Hg^{2+} + Pd^{2+}, S = Hg^{2+} + Na^{+}, T = Hg^{2+} + Cs^{+}, U = Hg^{2+} + Li^{+}, V = Hg^{2+} + Ba^{2+}, W = Hg^{2+} + Co^{2+}, X = Hg^{2+} + Sr^{2+}, Figure S20: Change in absorption spectra upon addition of 13.63μM mercuric ions in a solution of **1** (20 μM) in water at pH 7.0 (1.0 mM HEPES), Figure S21: Change in absorption spectra during titration of **1** ([**1**] = 20 μM) with copper ions in water at pH 7.0 (1.0 mM HEPES), Figure S22: Change in absorption spectra during titration of **1** ((**1**) = 20 μM) with chromium ions in water at pH 7.0 (1.0 mM HEPES), Figure 23: Change in absorption spectra during titration of **1** ((**1**) = 20 μM) with ferric ions in water at pH 7.0 (1.0 mM HEPES); Figure S24: Change in absorption spectra during titration of **1** ((**1**) = 20 μM) with aluminum ions in water at pH 7.0 (1.0 mM HEPES), Figure S24: A correlation between the observed absorbance and absorbance value calculated using the HypSpec program for a titration between **1** and copper ions with 1:1 (H:G) binding stoichiometry, Figure S25: A correlation between the observed absorbance and absorbance value calculated using the HypSpec program for a titration between **1** and chromium ions with 1:1 (H:G) binding stoichiometry, Figure S26: A correlation between the observed absorbance and absorbance value calculated using the program for a titration between **1** and ferric ions with 1:1 (H:G) binding stoichiometry, Figure S27: A correlation between the observed absorbance and absorbance value calculated using the HypSpec program for a titration between **1** and aluminum ions with 1:1 (H:G) binding stoichiometry, Figure S28: A comparison of the absorbance and fluorescence intensity for an equimolar solution of **1** and the mercuric ions, Figure S29: A partial ^{1}H-NMR spectra of **1** and **1**-Hg^{2+} showing a comparison in the aliphatic region, Figure S30: The ^{1}H-NMR spectra was recorded in DMSO-d_6 on a 400 MHz instrument; Figure S31: A partial ^{1}H-NMR spectra of **1** and **1**-Al^{3+} showing a comparison in the aromatic region. The ^{1}H-NMR spectra was recorded in DMSO-d_6 on a 400 MHz instrument, Figure 32: A partial ^{1}H-NMR spectra of **1** and **1**-Al^{3+} showing a comparison in the aliphatic region. The ^{1}H-NMR spectra was recorded in DMSO-d_6 on a 400 MHz instrument, Figure S33: The determination of limit of detection value of **1** towards mercuric ions using fluorescence spectroscopy, Figure S34: The DFT/PBE1PBE/6-31+G(d) optimized geometries of the different stereoisomers of **1**, Figure S35: The DFT/PBE1PBE/6-31+G(d) optimized geometries of the different stereoisomers of **1** in the zwitterionic form, Figure S36: The DFT/PBE1PBE/6-31+G(d) optimized geometries of the different stereoisomers of **1** in the protonated form, Figure S37: The DFT/PBE1PBE/6-31+G(d)/LANL2DZ optimized geometries of the **1**-Hg complex; Table S1: Experimental detail. Table S2: The contribution of different intermolecular interaction to

the total Hirshfeld surface; Table S3: The electronic excitation parameters for the receptors **1** and **1**-Hg^{2+} complex obtained calculated using TD-DFT/B3LYP/6-31G(d) method (Gaussian 09 A.02) in the gas phase.

Author Contributions: A.K. (Ajeet Kumar) and A.K. (Arvind Kumar) carried out the evaluation work. A.K. (Arvind Kumar) carried out the DLS studies. A.K. (Ajeet Kumar) and P.R.S. synthesized the receptor and characterized it using different techniques. S.K. solved the crystal data. All authors were involved in writing the manuscript.

Funding: The research was funded by a grant from DST-SERB (EMR/216/005022).

Acknowledgments: The authors are thankful to Pradeep Kumar (CSIR-IGIB) and Principal, St. Stephen's College for instrumental facilities and the necessary infrastructure. Authors are also thankful to Mr. KP for the help.

Conflicts of Interest: There is no conflict of interest associated with this manuscript.

References

1. Hylander, L.D.; Goodsite, M.E. Environmental costs of mercury pollution. *Sci. Total Environ.* **2006**, *368*, 352–370.
2. Li, P.; Feng, X.; Qiu, G.; Shang, L.; Li, Z. Mercury pollution in Asia: A review of the contaminated sites. *J. Hazard. Mater.* **2009**, *168*, 591–601.
3. Harris, H.H.; Pickering, I.J.; George, G.N. The chemical form of mercury in fish. *Science* **2003**, *301*, 1203–1203.
4. Hu, J.; Li, J.; Qi, J.; Chen, J. Highly selective and effective mercury (II) fluorescent sensors. *New J. Chem.* **2015**, *39*, 843–848.
5. Kim, H.N.; Ren, W.X.; Kim, J.S.; Yoon, J. Fluorescent and colorimetric sensors for detection of lead, cadmium, and mercury ions. *Chem. Soc. Rev.* **2012**, *41*, 3210–3244, doi:10.1039/C1CS15245A.
6. Boening, D.W. Ecological effects, transport, and fate of mercury: A general review. *Chemosphere* **2000**, *40*, 1335–1351.
7. Joensuu, O.I. Fossil fuels as a source of mercury pollution. *Science* **1971**, *172*, 1027–1028.
8. Gonzalez, H. Mercury pollution caused by a chlor-alkali plant. *Water Air Soil Pollut.* **1991**, *56*, 83–93, doi:10.1007/bf00342263.
9. Porcella, D.; Ramel, C.; Jernelov, A. Global mercury pollution and the role of gold mining: An overview. *Water Air Soil Pollut.* **1997**, *97*, 205–207.
10. Boischio, A.A.P.; Henshel, D. Fish Consumption, Fish Lore, and Mercury Pollution—Risk Communication for the Madeira River People. *Environ. Res.* **2000**, *84*, 108–126, doi:10.1006/enrs.2000.4035.
11. Okpala, C.O.R.; Sardo, G.; Vitale, S.; Bono, G.; Arukwe, A. Hazardous properties and toxicological update of mercury: From fish food to human health safety perspective. *Crit. Rev. Food Sci. Nutr.* **2018**, *58*, 1986–2001.
12. Obrist, D.; Agnan, Y.; Jiskra, M.; Olson, C.L.; Colegrove, D.P.; Hueber, J.; Moore, C.W.; Sonke, J.E.; Helmig, D. Tundra uptake of atmospheric elemental mercury drives Arctic mercury pollution. *Nature* **2017**, *547*, 201–204.
13. Krishna, P.; Basha, S.S.; Sathyavani, K.G.; Prabhavathi, K. Heavy metal bioaccumulation in the Channa marulius from Lake Kolleru and human health risk assessment. *Int. J. Zool. Stud.* **2018**, *3*, 76–79.
14. Li, J.; Li, X.; Wang, L.; Duan, Q. Advances in uptake, transportation and bioaccumulation of heavy metal ions in bivalves. *Shuichan Kexue* **2007**, *26*, 51–55.
15. Jackson, A.C. Chronic Neurological Disease Due to Methylmercury Poisoning. *Can. J. Neurol. Sci.* **2018**, *45*, 620–623.
16. Rice, K.M.; Walker, E.M.; Jr., Wu, M.; Gillette, C.; Blough, E.R. Environmental mercury and its toxic effects. *J. Prev. Med. Public Health* **2014**, *47*, 74–83, doi:10.3961/jpmph.2014.47.2.74.
17. Houston, M.C. Role of mercury toxicity in hypertension, cardiovascular disease, and stroke. *J. Clin. Hypertens.* **2011**, *13*, 621–627.
18. Dos Santos, A.A.; Chang, L.W.; Guo, G.L.; Aschner, M. Fetal Minamata Disease: A Human Episode of Congenital Methylmercury Poisoning. In *Handbook of Developmental Neurotoxicology*; Elsevier: San Diego, CA, USA, 2018; pp. 399–406.
19. Ancora, M.P.; Zhang, L.; Wang, S.; Schreifels, J.J.; Hao, J. Meeting Minamata: Cost-effective compliance options for atmospheric mercury control in Chinese coal-fired power plants. *Energy Policy* **2016**, *88*, 485–494.

20. Weiss, B. Why methyl mercury remains a conundrum 50 years after Minamata. *Toxicol. Sci.* **2007**, *97*, 223–225.
21. Nyanza, E.C.; Bernier, F.P.; Manyama, M.; Hatfield, J.; Martin, J.W.; Dewey, D. Maternal exposure to arsenic and mercury in small-scale gold mining areas of Northern Tanzania. *Environ. Res.* **2019**, *173*, 432–442, doi:10.1016/j.envres.2019.03.031.
22. Lin, J. Determination of heavy metals in sewages by microwave digestion coupled FAAS. *Fujian Fenxi Ceshi* **2007**, *16*, 84–86.
23. Racki, G.; Rakociński, M.; Marynowski, L. Anomalous Upper Devonian mercury enrichments: Comparison of Inductively Coupled Plasma–Mass Spectrometry (ICP-MS) and Atomic Absorption Spectrometry (AAS) analytical data. *Geol. Q.* **2018**, *62*, 487–495, doi:10.7306/gq1419.
24. Lech, T.; Turek, W. Application of TDA AAS to Direct Mercury Determination in Postmortem Material in Forensic Toxicology Examinations. *J. Anal. Toxicol.* **2019**, *43*, 385–391.
25. Murkovic, I.; Wolfbeis, O.S. Fluorescence-based sensor membrane for mercury (II) detection. *Sens. Actuator B Chem*. **1997**, *39*, 246–251.
26. Zhang, Y.; Gao, L.; Wen, L.; Heng, L.; Song, Y. Highly sensitive, selective and reusable mercury(II) ion sensor based on a ssDNA-functionalized photonic crystal film. *Phys. Chem. Chem. Phys.* **2013**, *15*, 11943–11949, doi:10.1039/c3cp51324f.
27. Zheng, G.C.; Wang, J.; Kong, L.T.; Cheng, H.F.; Liu, J.H. Cellular-Like Gold Nanofeet: Synthesis, Functionalization, and Surface Enhanced Fluorescence Detection for Mercury Contaminations. *Plasmonics* **2012**, *7*, 487–494, doi:10.1007/s11468-012-9333-9.
28. Sahoo, P.R.; Prakash, K.; Kumar, S. Light controlled receptors for heavy metal ions. *Coord. Chem. Rev.* **2018**, *357*, 18–49.
29. Crano, J.C.; Guglielmetti, R.J. *Organic Photochromic and Thermochromic Compounds: Volume 2: Physicochemical Studies, Biological Applications, and Thermochromism*; Springer: New York, NY, USA, 1999; Volume 2.
30. Sahoo, P.R.; Prakash, K.; Kumar, A.; Kumar, S. Efficient Reversible Optical Sensing of Water Achieved through the Conversion of H-Aggregates of a Merocyanine Salt to J-Aggregates. *Chem. Select* **2017**, *2*, 5924–5932, doi:10.1002/slct.201700940.
31. Rösch, U.; Yao, S.; Wortmann, R.; Würthner, F. Fluorescent H-Aggregates of Merocyanine Dyes. *Angew. Chem. Int. Ed.* **2006**, *45*, 7026–7030.
32. Möbius, D. Scheibe aggregates. *Adv. Mater.* **1995**, *7*, 437–444.
33. Sahoo, P.R.; Kumar, S. Synthesis of an optically switchable salicylaldimine substituted naphthopyran for selective and reversible Cu2+ recognition in aqueous solution. *RSC Adv.* **2016**, *6*, 20145–20154, doi:10.1039/C5RA24857D.
34. Kumar, S.; Velasco, K.; McCurdy, A. X-ray, kinetics and DFT studies of photochromic substituted benzothiazolinic spiropyrans. *J. Mol. Struct.* **2010**, *968*, 13–18, doi:10.1016/j.molstruc.2010.01.012.
35. Kumar, S.; Watkins Davita, L.; Fujiwara, T. A tailored spirooxazine dimer as a photoswitchable binding tool. *Chem. Commun.* **2009**, 4369–4371, doi:10.1039/B909496B.
36. Firdaus, M.L.; Aprian, A.; Meileza, N.; Hitsmi, M.; Elvia, R.; Rahmidar, L.; Khaydarov, R. Smartphone Coupled with a Paper-Based Colorimetric Device for Sensitive and Portable Mercury Ion Sensing. *Chemosensors* **2019**, *7*, 25.
37. Firdaus, M.L.; Alwi, W.; Trinoveldi, F.; Rahayu, I.; Rahmidar, L.; Warsito, K. Determination of Chromium and Iron Using Digital Image-based Colorimetry. *Procedia Environ. Sci.* **2014**, *20*, 298–304, doi:10.1016/j.proenv.2014.03.037.
38. Masawat, P.; Harfield, A.; Srihirun, N.; Namwong, A. Green Determination of Total Iron in Water by Digital Image Colorimetry. *Anal. Lett.* **2017**, *50*, 173–185, doi:10.1080/00032719.2016.1174869.
39. Schneider, C.A.; Rasband, W.S.; Eliceiri, K.W. NIH Image to ImageJ: 25 years of image analysis. *Nat. Methods* **2012**, *9*, 671–675, doi:10.1038/nmeth.2089.
40. Dolomanov, O.V.; Bourhis, L.J.; Gildea, R.J.; Howard, J.A.; Puschmann, H. OLEX2: A complete structure solution, refinement and analysis program. *J. Appl. Cryst.* **2009**, *42*, 339–341, doi:10.1107/S0021889808042726.
41. Sheldrick, G.M. SHELXT–Integrated space-group and crystal-structure determination. *Acta Cryst. A* **2015**, *71*, 3–8.

42. Macrae, C.F.; Bruno, I.J.; Chisholm, J.A.; Edgington, P.R.; McCabe, P.; Pidcock, E.; Rodriguez-Monge, L.; Taylor, R.; Streek, J.V., Wood, P.A. Mercury CSD 2.0–new features for the visualization and investigation of crystal structures. *J. Appl. Cryst.* **2008**, *41*, 466–470, doi:10.1107/S0021889807067908.
43. Frisch, M.J.; Trucks, G.W.; Schlegel, H.B.; Scuseria, G.E.; Robb, M.A.; Cheeseman, J.R.; Scalmani, G.; Barone, V.; Mennucci, B.; Petersson, G.A.; et al. *Gaussian 09, Revision A.02*; Gaussian, Inc.: Wallingford, CT, USA, 2009.
44. Wolff, S.; Grimwood, D.; McKinnon, J.; Jayatilaka, D.; Spackman, M. *Crystalexplorer 17.5*; University of Western Australia: Perth, Australia, 2018.
45. Thakuria, R.; Nath, N.K.; Roy, S.; Nangia, A. Polymorphism and isostructurality in sulfonylhydrazones. *CrystEngComm* **2014**, *16*, 4681–4690, doi:10.1039/C3CE42301H.
46. Gans, P.; Sabatini, A.; Vacca, A. Investigation of equilibria in solution. Determination of equilibrium constants with the HYPERQUAD suite of programs. *Talanta* **1996**, *43*, 1739–1753, doi:10.1016/0039-9140(96)01958-3.
47. Klajn, R. Spiropyran-based dynamic materials. *Chem. Soc. Rev.* **2014**, *43*, 148–184, doi:10.1039/C3CS60181A.
48. Adamo, C.; Barone, V. Toward reliable density functional methods without adjustable parameters: The PBE0 model. *J. Chem. Phys.* **1999**, *110*, 6158–6170, doi:10.1063/1.478522.